Electrochimica Acta 53 (2008) 8087–8100

Contents lists available at ScienceDirect

Electrochimica Acta

journal homepage: www.elsevier.com/locate/electacta

A dynamic performance model for redox-flow batteries involving soluble species

A.A. Shah*, M.J. Watt-Smith, F.C. Walsh

Energy Technology Research Group, School of Engineering Sciences, University of Southampton,
Highfields, University Road, Southampton SO17 1BJ, United Kingdom

ARTICLE INFO

Article history:
Received 11 January 2008
Received in revised form 24 March 2008
Accepted 24 May 2008
Available online 6 June 2008

Keywords:
Redox-flow battery
Vanadium redox cells
Energy storage
Energy conversion
Mathematical model

ABSTRACT

A transient modelling framework for a vanadium redox-flow battery (RFB) is developed and experiments covering a range of vanadium concentration and electrolyte flow rate are conducted. The two-dimensional model is based on a comprehensive description of mass, charge and momentum transport and conservation, and is combined with a global kinetic model for reactions involving vanadium species. The model is validated against the experimental data and is used to study the effects of variations in concentration, electrolyte flow rate and electrode porosity. Extensions to the model and future work are suggested.

1. Introduction

Modern demands for increasingly efficient energy delivery and the anticipated demand for renewable energy (the latter typically suffers from intermittency problems) have generated considerable interest in energy storage technologies. One of the most compelling of such technologies is the redox-flow battery (RFB). Unlike conventional batteries, such as lead-acid storage cells, in which energy is stored in the electrode structure, redox-flow batteries store energy in two solutions containing different redox couples with electrochemical potentials sufficiently separated from each other to provide an electromotive force to drive the reduction–oxidation reactions needed to charge and discharge the cell [1]. In theory, the capacity of the system is determined by the volume of the electrolyte tanks, while the system power is determined by the size of the stacks and the active electrode surface area. RFB technology enjoys several advantages over some of the established technologies such as static lead-acid batteries [1–3]:

1. high energy efficiencies (between 80% and 90% in large installations);
2. a low cost per kWh for large storage capacities;
3. existing systems can be readily upgraded and additional storage capacity easily installed by changing the tanks and volumes of electrolyte;
4. there is negligible hydrogen evolution during charging;
5. they are more “environmentally friendly” than alternatives that rely on heavy metals such as lead, nickel, zinc and cadmium, all of which have potentially adverse impacts during production, use and disposal;
6. RFBs can be fully discharged without harm to the battery;
7. the use of the same element in both half-cells avoids problems of cross-contamination during long-term use—solutions have indefinite life so that waste disposal issues are minimized;
8. they have a long cycle life and are relatively easily maintained;
9. some RFBs can be electrically recharged or mechanically refueled.

The potential applications of RFBs are numerous, including load levelling and peak shaving, uninterruptible power supplies, emergency backup (for example in hospitals and air-traffic control) and facilitation of wind and photovoltaic energy delivery [2,4].

In a true redox-flow battery, the reversible electrode processes involve soluble, solution-based redox species. Electrode processes take place at the surfaces of inert or catalyzed electrodes. The reactants flowing across these electrodes enter from reservoirs external to the electrochemical cell and the positively and negatively charged electrolytes are usually prevented from mixing in the electrochemical cell by an ion-selective membrane or micro-porous

---

* Corresponding author. Tel.: +44 23 8059 8520; fax: +44 23 8059 3131.
E-mail address: A.Shah@soton.ac.uk (A.A. Shah).

0013-4686/$ – see front matter © 2008 Elsevier Ltd. All rights reserved.
doi:10.1016/j.electacta.2008.05.067

separator. There are currently several types of RFB under development, each employing different redox couples. One of the most popular is the all-vanadium cell, first patented by Skyllas-Kazacos and Robins in 1986, [5], and further developed by Unisearch (University of South Wales in Australia) by Skyllas-Kazacos et al., [2,6,7]. Several commercial developers have invested heavily in this technology, including VRB Power Systems, Sumitomo Electric Industries (SEI), Energy for Sustainable Development Ltd. (ESD), V-Fuel Pty Ltd. and EN-o-DE Energy on Demand, and successful demonstration units have been piloted.[1]

The rapidly approaching commercialization of RFBs (the all-vanadium type in particular) sets a series of new challenges to developers of the technology, notably scale-up and optimization (with respect to flow geometries and operating conditions for example), improvement in electrolyte stability, development of electrode materials resistant to oxidation and mitigation of membrane fouling. Many of these challenges are not particularly well-suited to laboratory analysis alone by virtue of the associated financial costs and long timescales. In such cases it is natural to employ modelling and simulation as a means of down-selecting laboratory test scenarios so that, wherever possible, extensive laboratory experimentation can be avoided. However, in contrast to conventional batteries such as the lead-acid and lithium-ion [8–13], there are no models of the vanadium redox-flow battery of sufficient complexity to simulate experiment (even in the simplest case of one dimension and steady state). In this paper we develop a transient, two-dimensional model based on conservation principles (mass, momentum and charge), incorporating the fundamental modes of transport for the charged species and water. This transport model is combined with a kinetic model to simulate the performance of the all-vanadium RFB. The level of detail included is necessary for the model to form the basis of a practical simulation tool—often a major component in the design and testing strategies.

The next section contains details of the experimental work. Details of the model, including the underlying assumptions, are provided in Section 3. In Section 4 simulation results are presented, including comparisons to the experimental data and studies on the influence of vanadium concentration, flow rate and porosity of the carbon electrode. Finally, the results are summarized and future work is outlined.

2. Experimental details

The body of the redox-flow battery was constructed in polyvinyl chloride polymer. The positive and negative electrode compartments were 10 cm × 10 cm × 0.4 cm in size. The compartments, which were divided by a Nafion® 114 cation exchange membrane, were filled by porous and layered carbon felt electrodes (Sigratherm GFA5). The effective volumetric porosity of the felt electrodes was 0.68 ± 0.07. Electrolyte was circulated through each half-cell compartment through a glass reservoir (volume 250 mL, with a nitrogen gas atmosphere) and peristaltic pump circuit. The electrolyte contained a total vanadium concentration in the range 1000–1500 mol m^{-3}, as a V(III) and V(IV) mixture, in 4000 mol m^{-3} H_2SO_4, at a temperature of 297 ± 2 K. The volumetric flow rate was in the range 60–180 $\mathrm{cm}^3\,\mathrm{min}^{-1}$, corresponding to a mean linear flow velocity of 0.37–1.1 $\mathrm{cm\,s}^{-1}$ through the carbon felt electrodes. The cell was charged at a constant current (typically in the range 2–10 A, corresponding to a current density of 20–100 $\mathrm{mA\,cm}^{-2}$, based on the projected area of each electrode) and discharged at a constant voltage until a minimum voltage (typically 0.8 V) was achieved. Typically, the charge and discharge parts of a cycle were each 30–40 min in duration. Up to 30 cycles were used. An in-house personal computer and interface was used to monitor cell voltage. In addition, an open-circuit cell (divided by a Nafion® 1135 cation exchange membrane) was used to monitor the cell voltage between carbon rod electrodes (typically 8 mm diameter carbon rods). This cell effectively measured the differential redox potential between the half-cell electrolytes, which provided an indication of the state of charge of the electrolyte. The cell current was also monitored.

3. Model assumptions and equations

The kinetics associated with reduction and oxidation of vanadium species are known to be highly complex [14,15]. In this paper the following simplified set of half-reactions is adopted:

$$\text{Negative electrode}: \quad \mathrm{V(III)} + e^- \rightleftharpoons \mathrm{V(II)} \tag{1}$$

$$\text{Positive electrode}: \quad \mathrm{VO^{2+}} + \mathrm{H_2O} \rightleftharpoons \mathrm{VO_2}^{+} + 2\mathrm{H}^+ + e^- \tag{2}$$

There are several known “side reactions”, such as:

$$\begin{array}{l} 2\mathrm{H_2O} + 2e^- \rightleftharpoons \mathrm{H_2} + 2\mathrm{OH^-} \quad \text{hydrogen evolution} \\ 2\mathrm{H_2O} \rightleftharpoons \mathrm{O_2} + 4e^- + 4\mathrm{H^+} \quad \text{oxygen evolution} \\ \mathrm{VO^{2+}} + 2\mathrm{H_2O} \rightleftharpoons \mathrm{HVO_3} + 3\mathrm{H^+} + e^- \end{array} \tag{3}$$

and a number of others have been postulated [15]. Many species participate in the electrode reactions; in addition to the four vanadium species, water, components of a dissociated electrolyte (for example H^+, $HSO_4{}^-$and $SO_4{}^{2-}$in the case of sulfuric acid) can exist in the solutions at any one time [15]. In light of the uncertainty in the kinetics and a lack of characterization we focus attention on the “global” mechanism described by reactions (1) and (2).

The transport of each charged species, by diffusion, migration and convection, contributes to the current and affects the performance. Inclusion of all three transport mechanisms is, therefore, desirable. The fullest description of the battery system involves highly nonlinear terms and coefficients in a complex system of partial differential equations that couples the fluid dynamics and electrochemical phenomena. In order to formulate a manageable problem, it is usual in such cases to adopt certain simplifying assumptions regarding the transport processes. In the general case these assumptions depend primarily on the number of species considered and their relative concentrations. For example, the dilute-solution approximation can be employed in the case of a dominant component, or concentrated solution theory (based on the Maxwell–Stefan equations) for a completely dissociated salt in a binary solution [16]. Models of lead-acid [8], nickel-metal hydride [9,10] and lithium-based [11–13], batteries are typically based on a binary-electrolyte approximation, which is not applicable to the problem under consideration in this paper. In the case of a binary electrolyte concentrated-solution theory is straightforward but becomes cumbersome when several species are involved. Moreover, it requires values for several additional transport parameters that are not known for the present system.

It is also worth noting the similarities between the model developed below and fuel cell models, namely polymer–electrolyte (PEMFC) [17,18], and (single phase, saturated) direct-methanol [19,20]. Both the all-vanadium battery and the aforementioned fuel cell types employ a Nafion®-based membrane to transport charge (and as a by-product, water) from the positive to negative electrode. Models that have been developed for the transport of species in the membrane of a PEMFC are directly applicable to the present problem, and a particular model, namely that found in [21,22], will be employed for the membrane sub-model in this paper.

The model we develop is based on a two-dimensional slice as depicted in Fig. 1. All of the main components of the battery are

---

[1] Details can be found at http://www.vrbpower.com and http://www.sei.co.jp.

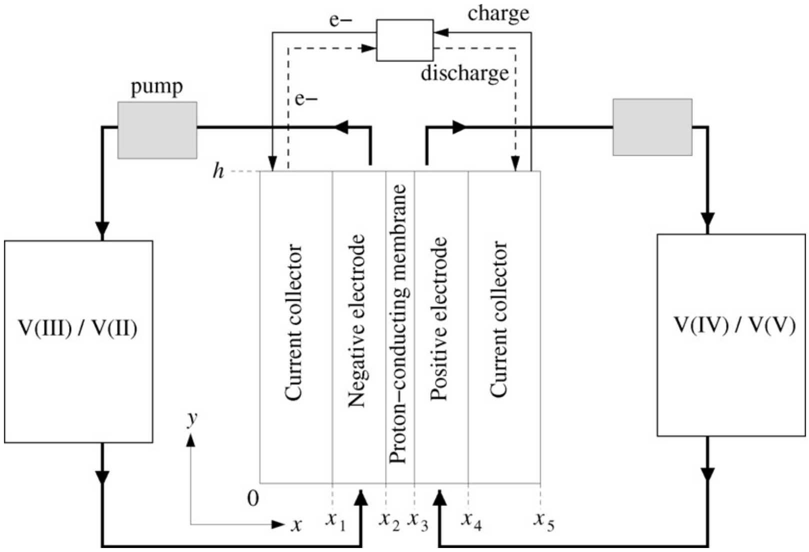

Fig. 1. A schematic of the all-vanadium battery and of the components modelled in this paper: current collectors, porous carbon electrodes, membrane and reservoirs.

modelled: current collectors, electrodes, membrane and reservoirs. The two-dimensional approximation leads to a considerable saving in simulation times without a major loss in accuracy if the electrolyte flow rate is reasonably high, as in normal operation. Extension of the model to three dimensions is straightforward.

We make two approximations regarding the fluid flow: (i) we use the dilute-solution approximation and (ii) we treat the fluid as incompressible. Both of these approximations can be justified by the fact that the bulk of the liquid is water. We also neglect the volume change resulting from a transfer of water between the electrodes through the membrane. For calculations over very long times these changes would need to be incorporated but on the timescales considered in the present study the transfer is of the order of one or two percent, and, therefore, is not significant.

3.1. Equations in the porous carbon electrode

The addition of sulfuric acid will, in the presence of water, lead to the formation of $SO_4{}^{2-}$. This negatively charged species and the bisulfate ions $HSO_4{}^{-}$are necessary to maintain electroneutrality in the electrolyte solution. We need only consider the bisulfate ions, since the concentration of $SO_4{}^{2-}$ can be determined from the condition of electroneutrality expressed later. Let c_i, $i \in \{\text{II},\text{III},\text{IV},\text{V},\text{H}_2\text{O},\text{H}^+,\text{HSO}_4^-\}$, denote the concentration of species i in liquid (II corresponds to V(II), with similar notation for the other vanadium species). A volume-averaged mass balance in the porous regions is expressed in the following form:

$$\frac{\partial}{\partial t}(\epsilon c_i) + \nabla \cdot \vec{N}_i = -S_i \tag{4}$$

where ϵ is porosity, and S_i is the source terms for species i, defined in Table 1 and discussed in the sequel.

Table 1
Sources and sinks for the liquid phase Eq. (4)

Source term	Positive electrode	Negative electrode
S_{II} (V(II) concentration equation)	–	$\nabla \cdot \vec{i}/F$
S_{III} (V(III) concentration equation)	–	$-\nabla \cdot \vec{i}/F$
S_{IV} (V(IV) concentration equation)	$\nabla \cdot \vec{i}/F$	–
S_{V} (V(V) concentration equation)	$-\nabla \cdot \vec{i}/F$	–
$S_{\text{H}_2\text{O}}$ (water concentration equation)	$\nabla \cdot \vec{i}/F$	–
S_{H^+} (proton concentration equation)	–	$-2\nabla \cdot \vec{i}/F$

For the concentration fluxes, $\vec{N}_i$, modified Nernst–Planck equations can be used [16,23], in which transport of a charged species is assumed to occur by hydrodynamic dispersion, electrokinetic effects (electro-phoresis and -osmosis) and convection. The total flux is:

$$\vec{N}_i = -D_i^{\text{eff}} \nabla c_i - \frac{z_i c_i D_i^{\text{eff}}}{RT} F \nabla \phi + \vec{v} c_i \tag{5}$$

where $\vec{v}$ is the superficial electrolyte velocity, ϕ is the ionic potential, and D_i^{eff} and z_i are the effective diffusion coefficient and valence for species i, respectively. The effective diffusion coefficient is derived from the free-space value, D_i, by a Bruggemann correction [24]:

$$D_i^{\text{eff}} = \epsilon^{3/2} D_i$$

The velocity $\vec{v}$ is given by Darcy's law, in which the Kozeny-Carman law is used for the hydraulic conductivity [25]:

$$\vec{v} = -\frac{d_f^2}{K\mu} \frac{\epsilon^3}{(1-\epsilon)^2} \nabla p \tag{6}$$

where p is the liquid pressure, μ is the dynamic viscosity of the liquid, d_f is a mean fibre diameter and K is the Kozeny-Carman constant for a fibrous medium. In keeping with the dilute-solution approximation and incompressibility assumption, we assume a constant value for μ, equal to the value for water.

The electrolyte is considered electrically neutral and is therefore governed by the condition:

$$\sum_i z_i c_i = 0. \tag{7}$$

Conservation of charge (the charge entering the electrolyte, $\vec{i}_e$, is balanced by the charge leaving the solid phase, $\vec{i}_s$) yields:

$$\nabla \cdot \vec{i}_e + \nabla \cdot \vec{i}_s = 0. \tag{8}$$

Note that an electro-osmotic term (as appears in the so-called Schloegl equation used later in the membrane) is absent in Eq. (6) as a result of the electroneutrality condition. The total current transferred from the solid phase to the electrolyte, $\nabla \cdot \vec{i} = \nabla \cdot \vec{i}_e = -\nabla \cdot \vec{i}_s$, is equal to the net (volumetric) rate of electrochemical reaction multiplied by Faraday's constant, F. The flow of a charged species i

gives rise to a current density:

$$\vec{i}_i = z_i F \vec{N}_i.$$

The total current density in the electrolyte then satisfies (invoking electroneutrality):

$$\vec{i} = \sum_i \vec{i}_i = -\kappa^{\mathrm{eff}} \nabla \phi - F \sum_i z_i D_i^{\mathrm{eff}} \nabla c_i \tag{9}$$

where the effective conductivity, κ^{eff}, is given by

$$\kappa^{\mathrm{eff}} = \frac{F^2}{RT} \sum_i z_i^2 D_i^{\mathrm{eff}} c_i \tag{10}$$

in which T is temperature and R is the molar gas constant.

The liquid velocity is related to the gradient in liquid pressure according to Eq. (6). The liquid pressure is determined from an overall (liquid) mass balance, which from the incompressibility assumption is:

$$\nabla \cdot \vec{v} = 0. \tag{11}$$

The velocity appearing in this equation is, strictly, the mass-averaged velocity, as opposed to the molar-averaged velocity in Eq. (5). However, under the dilute-solution approximation these two velocities are approximately equal (they are identical in the extreme case of infinite dilution). Combining Eqs. (6) and (11) we obtain:

$$-\frac{d_{\mathrm{f}}^2}{k\mu} \frac{\epsilon^3}{(1-\epsilon)^2} \nabla^2 p = 0. \tag{12}$$

In PEM fuel cell modelling a pseudo-steady state for proton and electron transport is typically assumed (justified in [26]); the same approach is adopted here. The electronic potential in the porous carbon electrode is given by Ohm's law:

$$-\sigma_s^{\mathrm{eff}} \nabla^2 \psi = -\nabla \cdot \vec{i} \tag{13}$$

where conservation of charge, as expressed by (8), is imposed and $\sigma_{\mathrm{s}}^{\mathrm{eff}}$ is the effective conductivity of the porous carbon electrode, obtained from the value for the solid material, σ_{s}, subject to a Bruggemann correction:

$$\sigma_{\mathrm{s}}^{\mathrm{eff}} = (1-\epsilon)^{3/2} \sigma_{\mathrm{s}}.$$

3.2. Equations in the membrane

For the transport processes in the proton-conducting membrane we use the formulation of Bernadi and Verbrugge [21,22]. Alternative models in the PEMFC literature are the widely used phenomenological model of Springer et al. [27], and the hybrid model of Weber and Newman [28,29]. The model of Bernadi and Verbrugge is the most appropriate when the membrane is close to fully saturated, as we can reasonably expect to be the case in the present problem. Moreover, it permits a straightforward coupling between the membrane and porous-electrode equations.

The concentration of water dissolved in the membrane, $c_{\mathrm{H_2O}}$, satisfies the mass balance:

$$\frac{\partial c_{\mathrm{H_2O}}}{\partial t} - \nabla \cdot \left(D_{\mathrm{w}}^{\mathrm{eff}} \nabla c_{\mathrm{H_2O}} \right) + \nabla \cdot (\vec{v} c_{\mathrm{H_2O}}) = 0 \tag{14}$$

in which $D_{\mathrm{w}}^{\mathrm{eff}}$ is the effective diffusion coefficient for water and $\vec{v}$ is the liquid velocity. The driving forces for the bulk flow are potential and pressure gradients.

In contrast to the electrolyte in the porous carbon electrode, the liquid in the membrane is not electro-neutral, if we assume the presence of only water and protons. However, electroneutrality holds in any elementary volume of the bulk membrane, when we take into account the fixed charge sites in the membrane structure (sulfonic acid groups in the case of Nafion®).

The velocity $\vec{v}$ is given by Schloegl's equation:

$$\vec{v} = -\frac{k_\phi}{\mu_{\mathrm{H_2O}}} F c_{\mathrm{H^+}} \nabla \phi - \frac{k_p}{\mu_{\mathrm{H_2O}}} \nabla p \tag{15}$$

for electrokinetic permeability k_ϕ, hydraulic permeability k_{p}, water viscosity $\mu_{\mathrm{H_2O}}$, and proton concentration $c_{\mathrm{H^+}}$. As before, p is the liquid pressure. The incompressibility assumption gives the following continuity equation for the liquid in the membrane:

$$\nabla \cdot \vec{v} = 0 \tag{16}$$

which yields an equation for p.

From the electro-neutrality condition the proton concentration satisfies:

$$c_{\mathrm{H^+}} = -z_{\mathrm{f}} c_{\mathrm{f}}$$

where c_{f} is the fixed charge site concentration in the membrane and z_{f} is the fixed site charge. The value of $c_{\mathrm{H^+}}$ is taken as constant. Since protons are the only mobile ions, the equation for current conservation is (using Eqs. (15) and (16)):

$$0 = \nabla \cdot \vec{i} = \nabla \cdot \vec{N}_{\mathrm{H^+}} = -\frac{F^2}{RT} D_{\mathrm{H^+}}^{\mathrm{eff}} c_{\mathrm{H^+}} \nabla^2 \phi \tag{17}$$

where $D_{\mathrm{H^+}}^{\mathrm{eff}}$ is the effective diffusion coefficient of the proton. The pressure equation becomes, using Laplace's equation for the ionic potential:

$$-\frac{k_p}{\mu_{\mathrm{H_2O}}} \nabla^2 p = 0. \tag{18}$$

3.3. Current collectors

The only equation required for the current collectors, in the absence of temperature variations (arising from ohmic heating and heat transfer to the surroundings) is that for the electronic potential, which is given by Ohm's law:

$$-\sigma_{\mathrm{coll}} \nabla^2 \psi = 0 \tag{19}$$

σ_{coll} is the electronic conductivity of the collectors. As a reasonable approximation, its value is taken to be constant.

3.4. Reaction kinetics

The most straightforward description of the reversible reactions taking place on the solid surfaces of the porous carbon electrode is the Butler–Volmer law. It is adopted here because the precise multistep reaction mechanism is not known and it is expected that the basic reversible redox features can be adequately captured with this form. Its use in other applications, such as PEM fuel cells, is widespread and it is known to yield qualitatively accurate results. The transfer current densities are therefore:

$$\begin{aligned}
\nabla \cdot \vec{i} &= \epsilon A F k_1 \left(c_{\mathrm{III}}^s\right)^{\alpha_{-,1}} \left(c_{\mathrm{II}}^s\right)^{\alpha_{+,1}} \left\{ \exp\left(\frac{\alpha_{+,1} F \eta_1}{RT}\right) - \exp\left(-\frac{\alpha_{-,1} F \eta_1}{RT}\right) \right\}, \\
\nabla \cdot \vec{i} &= \epsilon A F k_2 \left(c_{\mathrm{IV}}^s\right)^{\alpha_{-,2}} \left(c_{\mathrm{V}}^s\right)^{\alpha_{+,2}} \left\{ \exp\left(\frac{\alpha_{+,2} F \eta_2}{RT}\right) - \exp\left(-\frac{\alpha_{-,2} F \eta_2}{RT}\right) \right\},
\end{aligned} \tag{20}$$

for the negative and positive electrode, respectively. The various symbols in these expressions are defined as follows: A is the specific (per unit volume of catalyst layer) active surface area of the electrode (solid-liquid interface); k_1 and k_2 are the standard rate constants for reactions (1) and (2), respectively; $\alpha_{+,k}$ and $\alpha_{-,k}$ are the anodic and cathodic transfer coefficients, respectively; and η_1

Table 2
Default initial and boundary values

Symbol	Quantity	Value
T	Operating temperature (°C)	27
c^0_{III}	Initial V(III) concentration [a] ($\mathrm{mol\,m^{-3}}$)	1053
c^0_{II}	Initial V(II) concentration ($\mathrm{mol\,m^{-3}}$)	27
c^0_{IV}	Initial V(IV) concentration [a] ($\mathrm{mol\,m^{-3}}$)	1053
c^0_{V}	Initial V(V) concentration ($\mathrm{mol\,m^{-3}}$)	27
c^0_{d}	Initial water concentration ($\mathrm{mol\,m^{-3}}$)	4.2×10^3
$c_{\mathrm{HSO_4^-}}$	Initial HSO_4^- concentration [b] ($\mathrm{mol\,m^{-3}}$)	1200
$c^0_{\mathrm{H^+}}$	Initial H^+ concentration [b] ($\mathrm{mol\,m^{-3}}$)	1200
p_{out}	Negative electrode outlet pressure (kPa)	300
ω	Volumetric flow rate ($\mathrm{mL\,s^{-1}}$)	1
I	Current (A)	10

The concentration of SO_4^{2-} at all times (including $t = 0$) is determined by the condition of electroneutrality (7).

[a] This value is based on an initial state of charge of 5%.

[b] Estimate based on the value of c_{f}.

Table 3
Default values of the constants related to structure

Symbol	Quantity	Size
h	Electrode height (cm)	10
L_{t}	Carbon electrode thickness (mm)	4
L_{w}	Carbon electrode width (cm)	10
L_{m}	Membrane thickness (μm)	180
L_{c}	Collector thickness (mm)	6
ϵ	Carbon electrode porosity [a]	0.68
d_{f}	Carbon electrode fibre diameter [b] (μm)	10
d	Carbon electrode inter-fibre distance [b] (μm)	10
L_{w}	Electrode width (cm)	10
V_T	Electrolyte volume (half cell) (m)	250
a	Specific surface area: electrode [b] ($\mathrm{m^{-1}}$)	2×10^6

[a] Measured.

[b] Estimated.

and η_2 are the overpotentials in the negative and positive electrode, respectively. In the sequel we make the common approximation $\alpha_{\pm,k} = 1/2$, where the subscript $k = 1, 2$ refers to reaction (1) or (2) respectively . The overpotentials are defined as follows:

$$\eta_k = \phi_s - \phi_e - E_{0,k} \tag{21}$$

where $E_{0,k}$, $k = 1, 2$, are the open circuit potentials for reactions (1) and (2) respectively, estimated from the relevant Nernst equations:

$$E_{0,1} = E'_{0,1} + \frac{RT}{F}\log_{10}\left(\frac{c_{\mathrm{III}}}{c_{\mathrm{II}}}\right), \qquad E_{0,2} = E'_{0,2} + \frac{RT}{F}\log_{10}\left(\frac{c_{\mathrm{IV}}}{c_{\mathrm{IV}}}\right) \tag{22}$$

The equilibrium potentials $E'_{0,1}$ and $E'_{0,2}$ are given in Table 3. We have neglected changes in proton concentration in these expressions since they are low during typical charge/discharge cycles. Nevertheless, our approach does represent a step beyond the common assumption of constant open-circuit potential in detailed models of this kind.

Table 4
Default values of the constants related to electrochemistry

Symbol	Quantity	Size
k_1	Standard rate constant: reaction (1) [a]	$1.75 \times 10^{-7}\,\mathrm{m\,s^{-1}}$
k_2	Standard rate constant: reaction (2)	$3 \times 10^{-9}\,\mathrm{m\,s^{-1}}$ [15]
$\alpha_{-,1}$	Cathodic transfer coefficient: reaction (1) [b]	0.5
$\alpha_{+,1}$	Anodic transfer coefficient: reaction (1) [b]	0.5
$\alpha_{-,2}$	Cathodic transfer coefficient: reaction (2) [b]	0.5
$\alpha_{+,2}$	Anodic transfer coefficient: reaction (2) [b]	0.5
$E'_{0,1}$	Equilibrium potential: V(II)/V(III)	−0.255 V [31]
$E'_{0,2}$	Equilibrium potential: V(IV)/V(V)	1.004 V [31]
c_{f}	Fixed charge site (sulfonate) concentration	$1200\,\mathrm{mol\,m^{-3}}$ [21]
z_{f}	Charge of fixed (sulfonate) sites	−1

[a] Fitted parameter.

[b] Approximation.

Table 5
Default values for constants related to the transport of charge and mass

Symbol	Quantity	Size
D_{II}	V(II) diffusion coefficient in electrolyte	$2.4 \times 10^{-10}\,\mathrm{m^2\,s^{-1}}$ [32]
D_{III}	V(III) diffusion coefficient in electrolyte	$2.4 \times 10^{-10}\,\mathrm{m^2\,s^{-1}}$ [32]
D_{IV}	V(IV) diffusion coefficient in electrolyte	$3.9 \times 10^{-10}\,\mathrm{m^2\,s^{-1}}$ [32]
D_{V}	V(V) diffusion coefficient in electrolyte	$3.9 \times 10^{-10}\,\mathrm{m^2\,s^{-1}}$ [32]
$D_{\mathrm{H_2O}}$	Water diffusion coefficient in electrolyte	$2.3 \times 10^{-9}\,\mathrm{m^2\,s^{-1}}$ [33]
$D^{\mathrm{eff}}_{\mathrm{w}}$	Water diffusion coefficient in the membrane	$5.75 \times 10^{-10}\,\mathrm{m^2\,s^{-1}}$ [27]
$D^{\mathrm{eff}}_{\mathrm{H^+}}$	Proton diffusion coefficient in the membrane	$1.4 \times 10^{-9}\,\mathrm{m^2\,s^{-1}}$ [34]
$D_{\mathrm{HSO_4^-}}$	HSO_4^- diffusion coefficient in the membrane	$1.23 \times 10^{-9}\,\mathrm{m^2\,s^{-1}}$ [35]
$D_{\mathrm{SO_4^{2-}}}$	SO_4^{2-} diffusion coefficient in the membrane	$2.2 \times 10^{-10}\,\mathrm{m^2\,s^{-1}}$ [35]
K	Kozeny-Carman constant: porous electrode	5.55 [36]
k_ϕ	Electrokinetic permeability: membrane	$1.13 \times 10^{-19}\,\mathrm{m^2}$ [34]
k_p	Hydraulic permeability: membrane	$1.58 \times 10^{-18}\,\mathrm{m^2}$ [37]
$\mu_{\mathrm{H_2O}}$	Water viscosity	$10^{-3}\,\mathrm{Pa\,s}$
σ_{s}	Electronic conductivity of porous electrode [a]	$500\,\mathrm{S\,m^{-1}}$
σ_{coll}	Electronic conductivity of collectors [a]	$1000\,\mathrm{S\,m^{-1}}$

[a] Approximations.

The quantities c^s_i are vanadium-species concentrations at the liquid–solid interfaces in the porous regions, which are generally different from the bulk values due to additional transport resistance (from the bulk solution to the interfaces). They can be related to the bulk values, c_i, by approximately balancing the rate of reaction with the rate of diffusion of reactant to (or from) the electrode surface at steady state. For this purpose it is convenient to re-write the Butler–Volmer terms in a form that indicates linear dependence on the surface concentrations (using Eqs. (22) in (20)). For the positive electrode during charge, the balance is

$$\begin{aligned} c_{\mathrm{IV}} - c^s_{\mathrm{IV}} &= \frac{\epsilon k_1}{\gamma_{\mathrm{IV}}}\left\{c^s_{\mathrm{IV}}\exp\left(\frac{F(\psi-\phi-E'_{0,2})}{2RT}\right) - c^s_{\mathrm{V}}\exp\left(-\frac{F(\psi-\phi-E'_{0,2})}{2RT}\right)\right\},\\ c_{\mathrm{V}} - c^s_{\mathrm{V}} &= -\frac{\epsilon k_2}{\gamma_{\mathrm{V}}}\left\{c^s_{\mathrm{IV}}\exp\left(\frac{F(\psi-\phi-E'_{0,1})}{2RT}\right) - c^s_{\mathrm{V}}\exp\left(-\frac{F(\psi-\phi-E'_{0,1})}{2RT}\right)\right\}, \end{aligned} \tag{23}$$

where $\gamma_{\mathrm{IV}} = D_{\mathrm{IV}}/d$ and $\gamma_{\mathrm{V}} = D_{\mathrm{V}}/d$. δ is the average inter-fibre distance in the porous carbon electrode and, as before, D_i is the diffusion coefficient for species i in solution. The quantities γ_i,

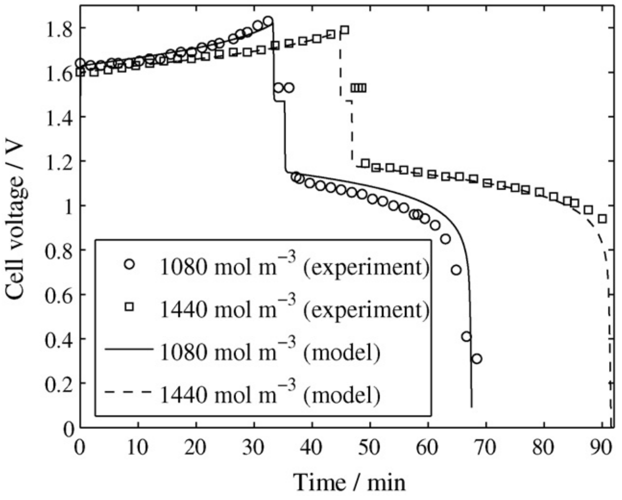

Fig. 2. A comparison of simulated and measured charge–discharge curves for $c^0_{\mathrm{III}} = 1080\,\mathrm{mol\,m^{-3}}$ and $c^0_{\mathrm{III}} = 1440\,\mathrm{mol\,m^{-3}}$. The charge times are 2017 s and 2714 s, respectively, and in each case 2 min at zero current were simulated before discharge. See Tables 2-5 for the other parameter values.

measuring the rate of reactant delivery to or from the surfaces by diffusion from the bulk, are the so-called “piston velocities” (in m s^{-1}). Solving these simultaneous equations for $c_{\rm IV}^{\rm s}$ and $c_{\rm V}^{\rm s}$ gives:

$$\begin{aligned} c_{\rm IV}^{\rm s} &= \frac{c_{\rm IV} + \epsilon k_2 {\rm e}^{-F(\psi-\phi-E'_{0,2})/2RT}\left(c_{\rm IV}/\gamma_{\rm V} + c_{\rm V}/\gamma_{\rm IV}\right)}{1+\epsilon k_2\left({\rm e}^{-F(\psi-\phi-E'_{0,2})/2RT}/\gamma_{\rm V} + {\rm e}^{F(\psi-\phi-E'_{0,2})/2RT}/\gamma_{\rm IV}\right)},\\ c_{\rm V}^{\rm s} &= \frac{c_{\rm V} + \epsilon k_2 {\rm e}^{F(\psi-\phi-E'_{0,2})/2RT}\left(c_{\rm IV}/\gamma_{\rm V} + c_{\rm V}/\gamma_{\rm IV}\right)}{1+\epsilon k_2\left({\rm e}^{-F(\psi-\phi-E'_{0,2})/2RT}/\gamma_{\rm V} + {\rm e}^{F(\psi-\phi-E'_{0,2})/2RT}/\gamma_{\rm IV}\right)}, \end{aligned} \tag{24}$$

These expressions are used in the reaction rates (20) to eliminate the surface concentrations in favour of the bulk values. Similar equations apply to the species at the negative electrode.

3.5. Initial-boundary conditions and parameter values

For the discussion on the boundary conditions we recall Fig. 1. At the interfaces between the membrane and electrodes, the species fluxes (excluding protons and water) and electron flux are considered to be negligibly small. At all external boundaries except the inlets and outlets the species fluxes are also zero, as is the flux of electrons along the top and bottom boundaries:

$$\vec{N}_i\cdot\vec{n} = 0 \quad \begin{cases} x = x_1,\ x = x_4 \\ x = x_2,\ x = x_3 \ \text{(except water/protons)} \\ y = 0,\ y = h \ \text{(except inlet/outlet)} \end{cases} \tag{25}$$

$$-\sigma_{\rm s}^{\rm eff}\nabla\psi\cdot\vec{n} = 0 \quad \begin{cases} x = x_2,\ x = x_3 \\ y = 0,\ y = h \end{cases} \tag{26}$$

The proton flux at the interfaces between the current collectors and electrodes in the x direction is zero:

$$\begin{aligned} &-\nabla\cdot\left(\kappa^{\rm eff}\nabla\phi + F\sum_i z_i D_i^{\rm eff}\nabla c_i\right)\cdot\vec{n} = 0 && x = x_1,\ x = x_4 \\ &-\frac{F^2}{RT}D_{\rm H^+}^{\rm eff}c_{\rm H^+}\nabla\phi\cdot\vec{n} = 0 && y = 0,\ y = h \\ & && \text{(membrane region)} \end{aligned} \tag{27}$$

The proton flux across the membrane in the x direction is of course nonzero. At the interfaces between the electrodes and membrane the proton concentration is constrained to satisfy $c_{\rm H^+} = c_{\rm f}$.

At all boundaries of the domain of integration of the pressure equation (except at the inlets and outlets) a Neumann condition is applied:

$$\nabla p\cdot\vec{n} = 0 \quad \text{(except inlets/outlets)} \tag{28}$$

At the inlets, each species enters with a prescribed bulk velocity and a concentration that depends on the pump rate (see below):

$$c_i = c_i^{\rm in}(t), \qquad v_y = v_{\rm in} \quad \text{(inlets)} \tag{29}$$

At the outlets, the liquid pressure is prescribed and all diffusive fluxes are set to zero (except pressure):

$$-D_i^{\rm eff}\nabla c_i\cdot\vec{n} = 0, \qquad p = p_{\rm out} \quad \text{(outlets)} \tag{30}$$

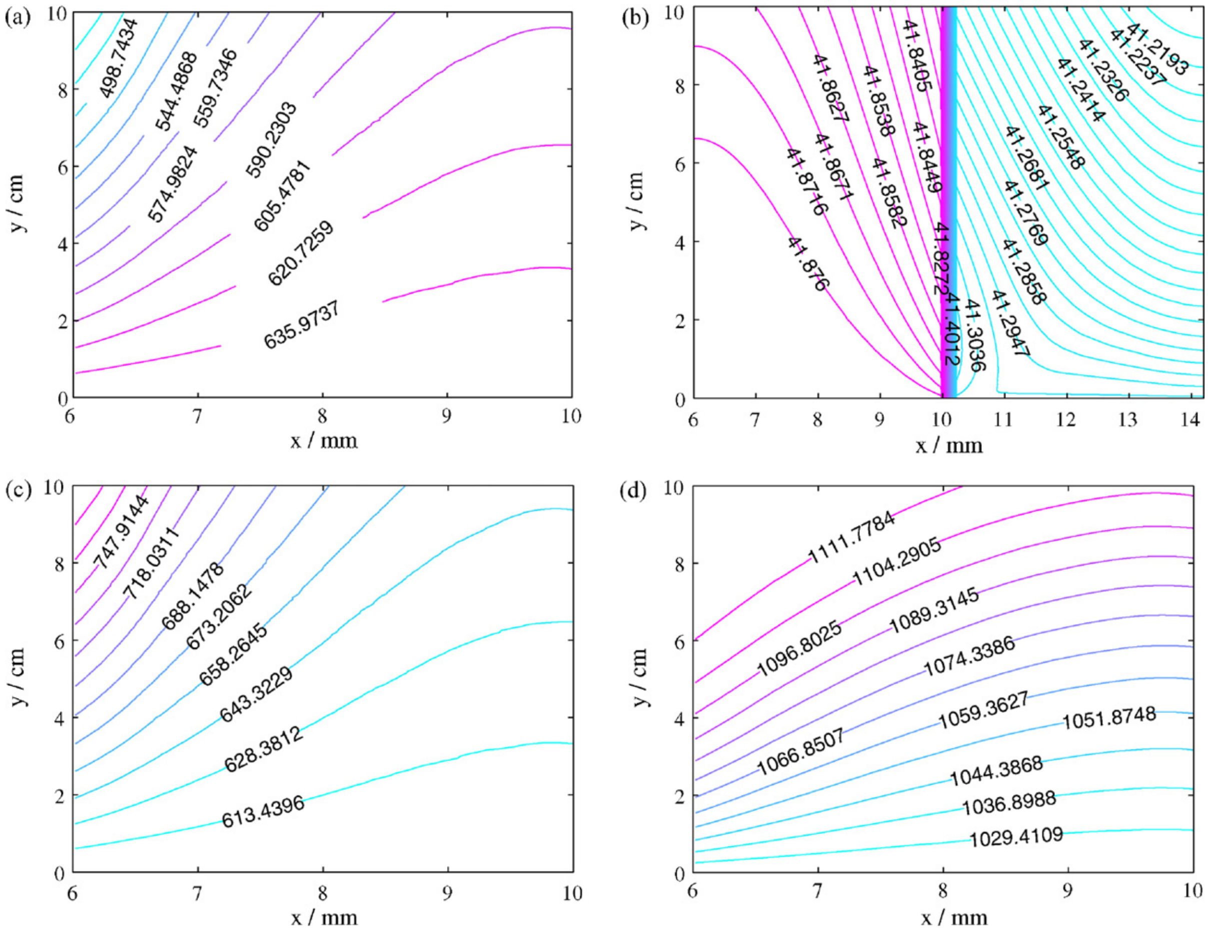

Fig. 3. Contours of the V(III) concentration during charge ((a) and (b)) and during discharge ((c) and (d)) corresponding to the cycle shown in Fig. 2. In this example $c_{\rm III}^0 = c_{\rm IV}^0 = 1080\,{\rm mol\,m^{-3}}$. Referring to Fig. 1, the line $x_1 = 6$ mm represents the current-collector/electrode interface and $x_2 = 10$ mm represents the membrane/electrode interface.

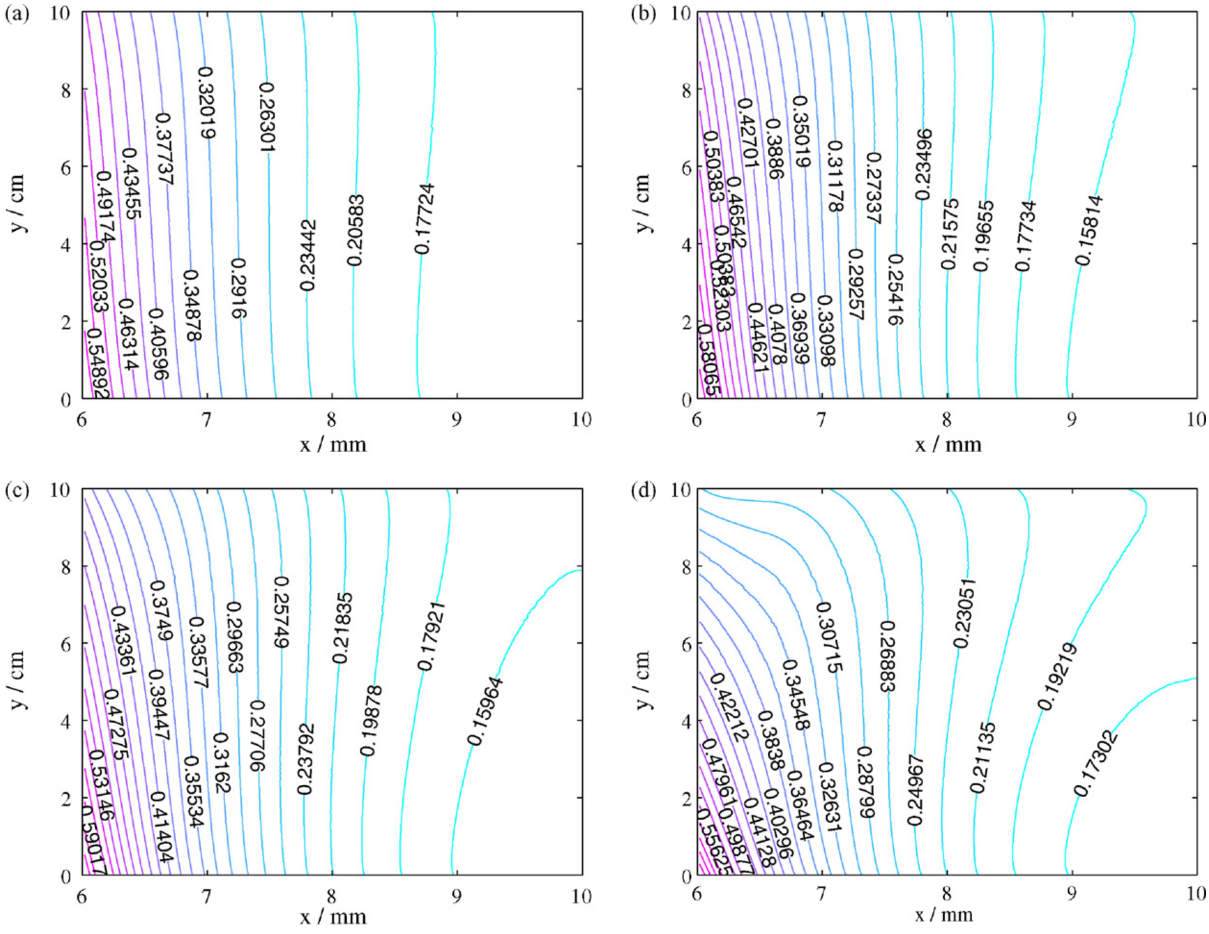

Fig. 4. Evolution of the (magnitude of the) transfer current density during charge in the negative electrode for the case $c^0_{\rm III} = c^0_{\rm IV} = 1080\,{\rm mol\,m^{-3}}$ in Fig. 2. Referring to Fig. 1, the line $x_1 = 6$ mm represents the current-collector/electrode interface and $x_2 = 10$ mm represents the membrane/electrode interface.

The remaining boundary conditions on the electronic potential depend on whether the battery is operated in potentiostatic or galvanostatic mode. For the present galvanostatic case the current is assumed to enter or leave uniformly through the current collectors, manifested through the following flux conditions (during charge):

$$-\sigma_{\rm coll}\nabla\psi\cdot\vec{n} = \begin{cases} -\dfrac{I}{a} & x = 0 \\ \dfrac{I}{a} & x = x_5 \end{cases} \tag{31}$$

where I is the current and a is the surface area to which the current is applied. For discharge the signs are reversed.

Consistent initial conditions are prescribed for the concentrations and potentials as follows:

$$\begin{array}{llll} \text{negative electrode} & c_i(t=0) = c_i^0 & \psi(t=0) = E_{0,1}(t=0) & \phi(t=0) = 0 \\ \text{positive electrode} & c_i(t=0) = c_i^0 & \psi(t=0) = E_{0,2}(t=0) & \phi(t=0) = 0 \end{array} \tag{32}$$

In the experimental arrangement the cell voltage (current flowing) is measured from the potential difference across an open-circuit cell, i.e., with conditions pertaining to the cell outlets. In the simulations the cell voltage, E, was measured with respect to the potentials at the intersections between the current collectors and electrodes, along $y = h$ in Fig. 1.

The default set of parameter values for the simulations is given in Tables 2–5. These values were used unless otherwise stated.

3.6. *Pump approximation and inlet conditions*

In the real system the movement of the electrolyte solution through the electrode and pump alters the concentrations at the inlet boundaries with time. It is essential to capture at least the main features of this process since the flow rate is the main variable used to control the distribution of electrolyte and can markedly affect the performance of the battery (as demonstrated below).

Invoking conservation of volume, the volumetric flow at the outlet boundaries, with cross-sectional area $A_{\rm out}$, is $\omega = v_{\rm in}\epsilon A_{\rm out}$. From the calculated average concentration at the outflow boundaries, $c_i^{\rm out}$ (found by integrating along the outlet surface), the inlet concentrations are approximated from the following mass balance, which assumes instantaneous mixing and negligible reaction in the reservoir of volume V:

$$\frac{{\rm d}c_i^{\rm in}}{{\rm d}t} = \frac{\omega}{V}\left(c_i^{\rm out} - c_i^{\rm in}\right), \quad c_i^{\rm in}(0) = c_i^0 \tag{33}$$

where, as defined above, c_i^0 is the initial concentration of species i (water, vanadium species, protons and anions). The total volume of electrolyte on each side of the battery, V_T, is the sum of the electrode and the reservoir volumes, $\epsilon hL_{\rm t}L_{\rm w}$ and V, respectively, where h is the height of the porous carbon electrode, $L_{\rm t}$ its thickness and $L_{\rm w}$ its width (see Table 3 for values). The volume in the pipes was assumed to be negligible.

3.7. Numerical details

The model presented above was solved using the package COMSOL Multiphysics® with a combination of the convection-diffusion, general-form and ODE options. The package is based on the finite-element method; a quadratic basis was used in all of the simulations, together with a minimum of 2548 elements and a maximum of 7256 elements. The relative error tolerance was set to 1×10^{-8}.

In order to match the potential at the beginning of charge it was necessary to take into account the contact resistances between the electrode and current collectors. A total value of 131 mV. was obtained from fitting the experimental to simulation results. The entire cell voltage curve in each calculation was shifted vertically upwards by this value. A second fitting parameter was the standard rate constant k_1, for a which a value of 1.75×10^{-7} m s^{-1} was used. Note that these quantities were fitted only once (in the first simulation) and subsequently used for all calculations.

4. Results and discussion

4.1. Concentration effects

Experiments were carried out at two different concentrations and electrolyte inflow rates. The state of charge (SOC) in the simulations was measured from the residual V(III) concentration:

$$1 - \frac{c_{\rm av}}{c^0_{\rm III}}$$

where zero corresponds to a zero SOC and unity to a full SOC. The quantity $c_{\rm av}$ is the average V(III) concentration in the negative half-cell, including both the electrode and reservoir volumes, found by a volume average. For each case, the SOC value at the end of the charging period was estimated from simulation to be 0.794 based on the experimental charge time for $c^0_{\rm III} = c^0_{\rm IV} = 1080\,{\rm mol\,m^{-3}}$, i.e., we used the same charge time in the simulation and measured the value of SOC as defined above. At the end of the charge period, 2 min of operation at zero current followed by discharge were simulated in each calculation.

Fig. 2 shows a comparison between the simulations and experiments for two different concentrations, $c^0_{\rm III} = c^0_{\rm IV} = 1080\,{\rm mol\,m^{-3}}$ and $c^0_{\rm III} = c^0_{\rm IV} = 1440\,{\rm mol\,m^{-3}}$, demonstrating that the model captures the trends extremely well. Both sets of results show an increased coulombic efficiency for increased concentration. In the calculations, the charge times (to reach an equivalent state of charge) are, approximately, 2017 s and 2714 s for the two cases $c^0_{\rm III} = 1080\,{\rm mol\,m^{-3}}$ and $c^0_{\rm III} = 1440\,{\rm mol\,m^{-3}}$, respectively. The small discrepancies in cell voltage between the experiments and simulations are likely to be due to the known presence of side reactions, which are not accounted for in the present model but are explored in a forthcoming paper. We have chosen not to fit the simulation results to the data for this reasons, and since our primary interest is in capturing the trends.

Faraday's law states that the concentration change in V(III) for a spatially homogeneous system of volume V_T, Δc, is related to the time of charging, t_c, and the current, I, as follows

$$-\frac{It_c}{F} = \Delta n = V_T \Delta c = -V_T c_0 \left(1 - \frac{c}{c_0}\right) \tag{34}$$

where $1 - c/c_0$ is a normalized concentration change, corresponding to an initial concentration c_0, and n is the number of moles. The time to reach a given SOC (or $1 - c/c_0$) for a given current and volume is therefore directly proportional to the initial concentration. If we employ the average concentration $c_{\rm av}$ as the concentration c in Eq. (34), the estimated concentration change in V(III) for the case $c^0_{\rm III} = 1080\,{\rm mol\,m^{-3}}$is $\Delta n = It/F = 0.209$ mol. The normalized concentration change is therefore $1 - c/c_0 = \Delta n/(V_T c_0) = 0.794$, which is identical to the simulated value of 0.794. Moreover, the ratio of charge times for the two cases in Fig. 2 can be estimated as $1.44/1.08 = 1.33$, which is almost identical to the value of $2714/2017 = 1.346$ yielded by the calculations.

Contour plots of the V(III) concentration at times during charge and discharge for the case $c^0_{\rm III} = 1080\,{\rm mol\,m^{-3}}$ are shown in Fig. 3. In these plots, $x = 6$ mm corresponds to x_1 in Fig. 1 and $x = 10$ mm corresponds to x_2. The inlet surface is represented by the line $y = 0$ and the outlet by $y = 10$ cm. During charge (Figures (a) and (b)) the depletion of V(III) increases as the height above the inlet surface increases along any vertical line. The degree of variation in this direction is determined primarily by the rate at which the electrolyte is moved through the electrode via the pump, i.e. the volumetric flow rate ω, and, as we would expect, the greatest concentration occurs along the inlet surface. Along any horizontal line the depletion of V(III) during charge increases as the current collector surface ($x = 6$ mm) is approached, since it is the surface along which the current enters. At both times the minimum value of

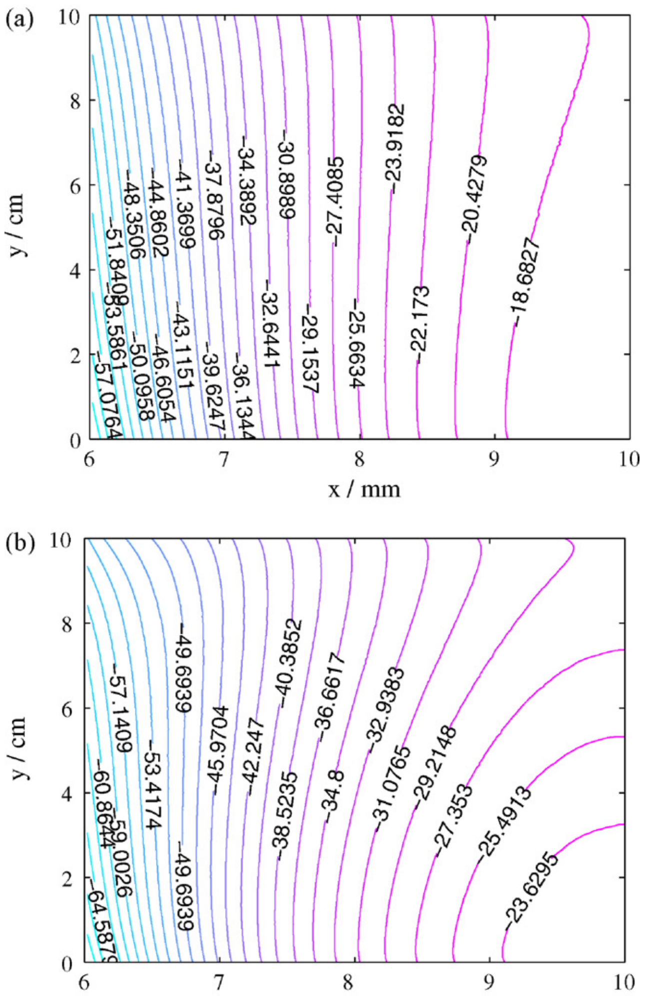

Fig. 5. Simulated contours of overpotential in the negative electrode during charge for the case $c^0_{\rm III} = 1080\,{\rm mol\,m^{-3}}$. Referring to Fig. 1, the line $x_1 = 6$ mm represents the current-collector/electrode interface and $x_2 = 10$ mm represents the membrane/electrode interface.

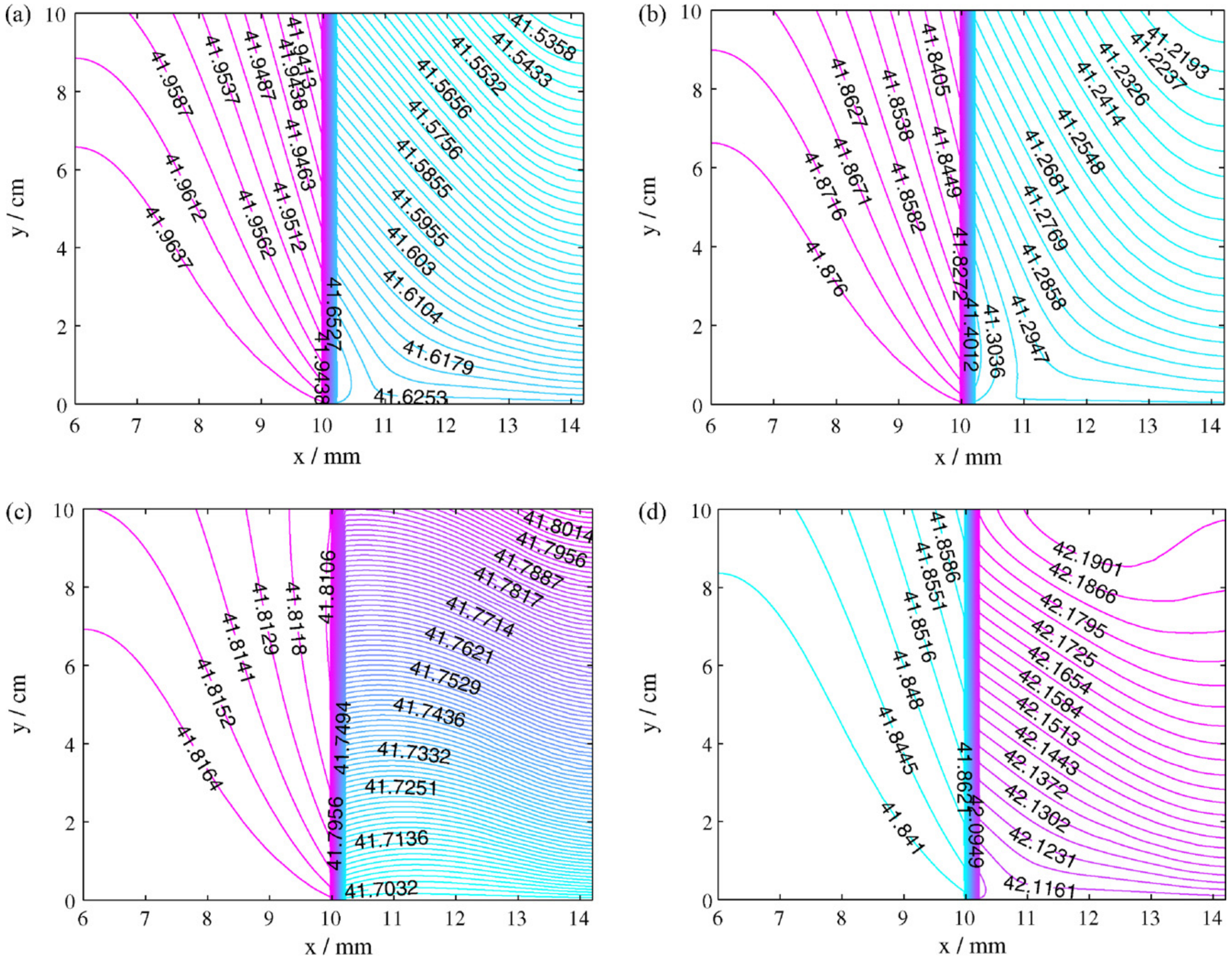

Fig. 6. Evolution of the water concentration during the charge and discharge cycle in the case $c^0_{\mathrm{III}} = c^0_{\mathrm{IV}} = 1080\,\mathrm{mol\,m^{-3}}$. See Tables 2–5 for other parameter values. Referring to Fig. 1, $x_1 = 6\,\mathrm{mm}$, $x_2 = 10\,\mathrm{mm}$, $x_3 = 10.18\,\mathrm{mm}$ and $x_4 = 14.18\,\mathrm{mm}$. There is a net transport of water from the positive electrode to negative electrode during charge, with the converse being true during discharge.

V(III) concentration therefore lies at the intersection of the upper surface, $y = 10\,\mathrm{cm}$, and the electrode/current-collector interface, $x = 6\,\mathrm{mm}$. These effects are mirrored in the V(II) concentration during discharge, the evolution of which can be deduced form the V(III) profiles shown on the bottom row. Moreover, we found a similar pattern in the positive electrode, where the minimum concentration of V(IV) occurs at the intersection of the outlet and current collector (during charge). To conserve space these are not shown.

Fig. 4 shows the evolution of the transfer current density in the negative electrode (given in Eq. (20)) during charge. The maximum current density, and therefore maximum reaction rate at all times during charge (Figures (a) and (b)) occurs at the intersection of the inlet and current collector surface ($x = 6$ mm, $y = 0$), where the concentration is highest and the current enters. Also noticeable from these plots is that the current density falls sharply at the end of the charge cycle along the outlet surface where the outlet and current collector intersect ($x = 6\,\mathrm{mm}$, $y = 10\,\mathrm{cm}$) and increases along the outlet in the vicinity of the membrane ($x = 10\,\mathrm{mm}$, $y = 10\,\mathrm{cm}$). A small decrease can also be seen at $x = 6\,\mathrm{mm}$, $y = 0$, where the inlet and current collector intersect, and a small increase at $x = 10\,\mathrm{mm}$, $y = 0$, where the inlet surface meets the membrane. Referring back to Fig. 3, reaction depletion appears to be the cause of this pattern; notice in particular that the current density (which is a function of the reactant concentrations and overpotential) fall most sharply where the reactant concentration attains its minimum. Fig. 5 shows the corresponding contours of overpotential in the negative electrode during charge. The overpotential drops quite sharply in most regions in order to maintain the current, particularly in the upper half of the electrode as the membrane ($x = 10$ mm) is approached. The drop is not as steep near $x = 6\,\mathrm{mm}$, $y = 10\,\mathrm{cm}$, where reaction is severely limited by the V(III) concentration. Knowledge of the location and extent of such polarization is vital in preventing or mitigating the effects of side reactions such as oxygen and hydrogen evolution. Even though side reactions are not incorporated, the onset of these reactions can be predicted by the model.

Fig. 6 shows the simulated profiles of water concentration during charge (Figures (a) and (b)) and discharge (Figures (c) and (d)) for the case $c^0_{\mathrm{III}} = c^0_{\mathrm{IV}} = 1080$ $\mathrm{mol\,m^{-3}}$. As before, $x = 6\,\mathrm{mm}$ corresponds to the current-collector/negative-electrode interface and $x = 10\,\mathrm{mm}$ to the negative-electrode/membrane interface. The region $10\,\mathrm{mm} < x < 10.18\,\mathrm{mm}$ corresponds to the membrane and $10.18\,\mathrm{mm} < x < 14.18\,\mathrm{mm}$ corresponds to the positive electrode. The model predicts a net transfer of water from the negative to positive electrode during charge (the net effect of the migration

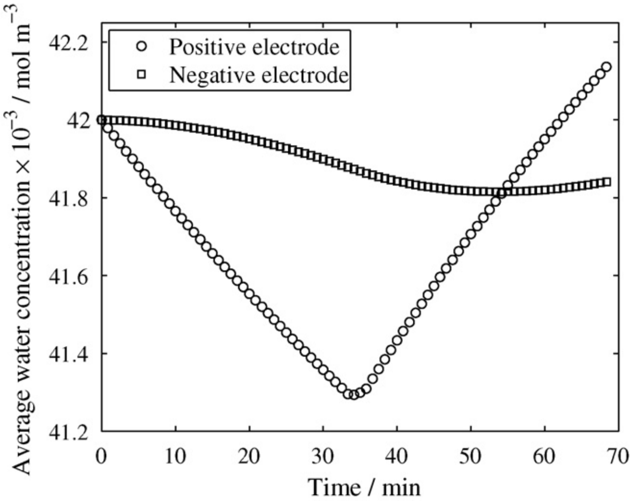

Fig. 7. Evolution of the average water concentration (over both the electrode and reservoir) in the negative and positive electrodes during the charge–discharge cycle for the case $c^0_{\rm III} = 1080\ \text{mol m}^{-3}$. Fig. 6 shows corresponding profiles of the water concentration at selected times.

of hydrated protons and transport due to concentration and pressure gradients). During discharge the net transfer is initially from the negative to positive electrode but towards the end of the cycle reverses direction. From Fig. 6(a) and (b) it appears that drag of water from the positive to negative electrode is not the dominant mechanism of transport, but rather back diffusion, which is caused by the developing concentration and liquid-pressure gradients from the negative to positive electrode. The magnitude of the drag coefficient depends on the current density, which in this example is low. For increasing current densities we would expect the rate of water transfer from the positive to negative electrode to increase, and for high enough current densities the drag to become dominant.

Fig. 7 shows the evolution of the average water concentrations in both electrodes (including both the reservoir and electrode volumes) during the charge–discharge cycle, confirming the picture described above. Note that the profiles for the average concentrations in the electrodes alone have identical shapes. In the positive electrode water is consumed during charge, which, combined with the drag, forces the water concentration to decrease with time. This explains the dominance of back diffusion during charge. On discharge water is produced in the positive electrode. The existing pressure and concentration gradients combined with drag, now from the negative to positive electrode, ensure that water continues to be transferred from the negative to positive electrode. Eventually, the concentration gradient that develops from the positive to negative electrode is sufficient to overcome the drag of water in the opposite direction. This can be seen in the average water concentration in the negative electrode from approximately $t = 55$ min onwards. At the end of discharge, at which time the initial state of charge is recovered, there is a net increase in water concentration in the positive electrode and a net decrease in the negative electrode, relative to the initial concentrations.

On the timescales of the present calculations the net water transfer is relatively small, but over long times can cause substantial volume changes in the reservoirs [30], leading to dilution of vanadium concentrations or conversely supersaturation and crystallization. Keeping track of the water content is important and changes can be captured, and more easily visualized, from a model that incorporates the water transport mechanisms.

4.2. *Effects of inlet flow rate*

An important control mechanism in the operation of a VRB system is the flow (pump) rate of the electrolyte. If the flow rate is too low the electrolyte is not efficiently circulated and stagnant regions will form in the electrode. On the other hand, a flow rate that is too high runs the risk of leakage or may not yield sufficient performance gains for the extra power required. Fig. 8 compares simulation results with experimental data at two volumetric flow rates in the case $c^0_{\rm III} = 1080\ \text{mol m}^{-3}$. Both the trend and the magnitude of change are captured well. These results suggest that as the flow rate is increased the coulombic efficiency improves. The third simulation result ($\omega = 3\,\text{mL s}^{-1}$) suggests that the relative gain in coulombic efficiency decreases as the flow rate is increased, which in turn suggests (as confirmed by experiment) that there is a flow rate of optimum performance versus the volumetric flow.

Fig. 9 shows contours of the V(III) concentration, current density and overpotential in the negative electrode at the end of the

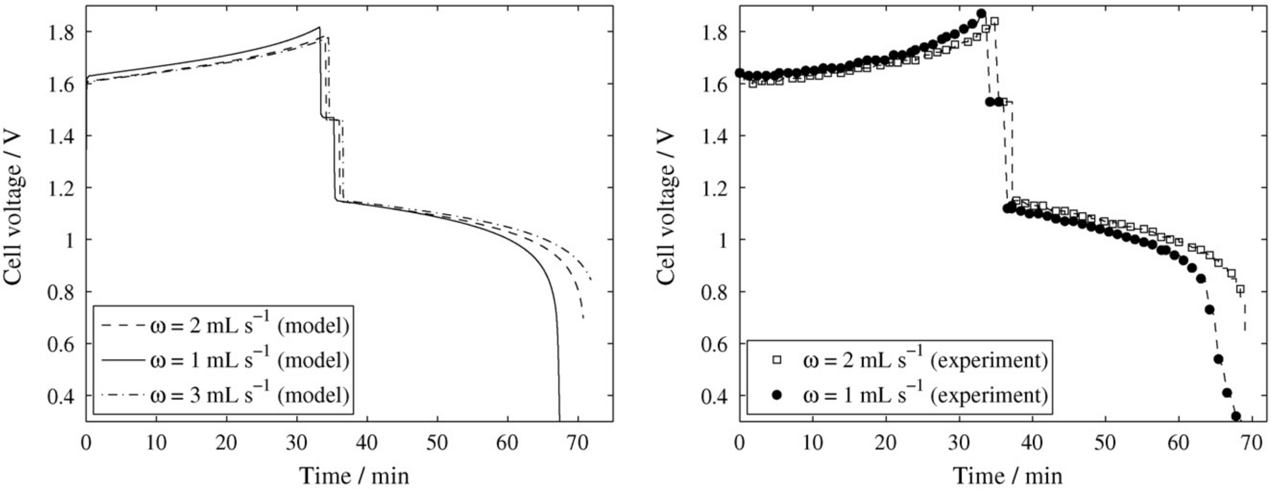

Fig. 8. A comparison of simulated and measured charge–discharge curves for two volumetric flow rates, with $c^0_{\rm III} = 1.08\,\text{mol dm}^{-3}$. The charge times are 2017 s for $\omega = 1\,\text{mL s}^{-1}$ and 2045 s for $\omega = 2\,\text{mL s}^{-1}$, and in each case 2 min at zero current were simulated before discharge. See Tables 2–5 for the other parameter values.

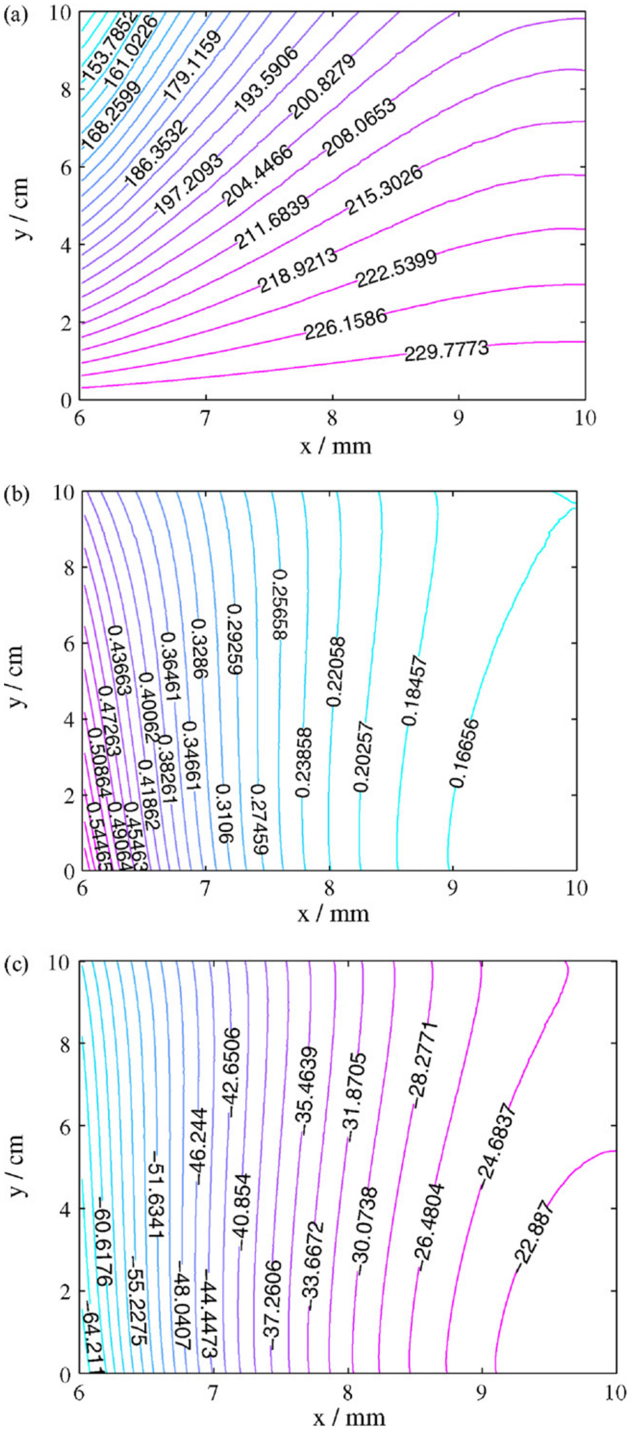

Fig. 9. Simulated contours of V(III) concentration, transfer current density and overpotential in the negative electrode at $t = 2045$ s (end of charge) for $\omega = 2\,\mathrm{mL\,s^{-1}}$ with $c^0_{\mathrm{III}} = 1080\,\mathrm{mol\,m^{-3}}$. Referring to Fig. 1, the line $x_1 = 6$ mm represents the current-collector/electrode interface and $x_2 = 10$ mm represents the membrane/electrode interface. Compare with the equivalent contour plots in Figs. 3-5.

discharge period at $t \approx 2045$ s (of equivalent SOC to the calculations depicted in Fig. 3) for $\omega = 2\,\mathrm{mL\,s^{-1}}$. When compared to Figs. 3 and 5, in which $\omega = 1\,\mathrm{mL\,s^{-1}}$, it is clear that the concentration in the electrode is more evenly distributed at the higher flow rate. The overpotential and transfer current density are in turn more evenly distributed. A higher flow rate reduces the contact time for reaction in the electrode, which leads to a slightly longer time for the exit solution to reach the desired state of charge. This also explains the greater degree of uniformity in the concentration (the reactant in the electrode is replenished from the reservoir more rapidly), and why the cell voltage at the end of charge is slightly lower.

To summarize, these results suggest two main benefits to a high (optimal) flow rate: increased coulombic efficiency and lower rates of hydrogen and oxygen evolution.

4.3. Variations in electrode porosity

There are various criteria for selecting the electrode material, such as electrical conductivity, resistance to corrosion and specific surface area, the latter depending on the micro-structure and porosity. As a final demonstration of the capabilities of the model we refer to Fig. 10, which shows simulated charge–discharge curves for three porosity values (the value in all previous figures is $\epsilon = 0.68$). Note that the total volume of electrolyte was the same in all cases. The differences in the curves in Fig. 10 are quite marked, even for these relatively small differences in porosity.

There are several effects associated with an increased porosity: decreased bulk conductivity, increased bulk diffusion coefficients, increased permeability and greater electrolyte volume in the electrode. The increasing volume in the electrode leads to an increased bulk reaction rate and therefore a more rapid depletion of V(III) during charge at any fixed time, as can be seen from the contour plots in Fig. 11. The V(III) concentration is much more uniform throughout the electrode for $\epsilon = 0.6$, as are the current density and overpotential, the latter of which is significantly higher on average. The lower concentration of V(III) and the decreased bulk conductivity (by a factor of approximately 3) for $\epsilon = 0.8$ lead to greater polarization. A higher porosity would therefore lead to increased rates of side reactions during charging.

As is evident from Fig. 11, the lower bulk reaction rate in going from $\epsilon = 0.8$ to $\epsilon = 0.6$ significantly increases the time taken to reach an equivalent state of charge, as well as the coulombic efficiency (the charge times are 2311 s for $\epsilon = 0.6$, 2017 s for $\epsilon = 0.68$ and 1796 s for $\epsilon = 0.8$). The degree of performance improvement is similar to that due to an increase in the concentration of V(III) by one third, as is seen by comparing Fig. 10 to Fig. 2.

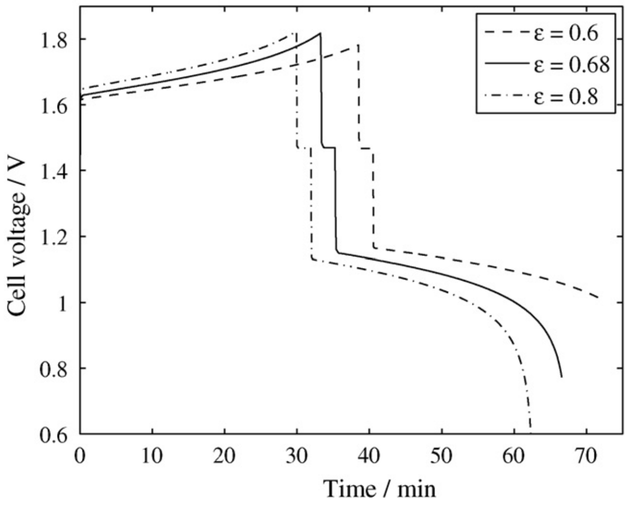

Fig. 10. Simulated charge–discharge curves for three electrode porosity values ($\epsilon = 0.68$ corresponds to the base case), with $c^0_{\mathrm{III}} = 1080\,\mathrm{mol\,m^{-3}}$. The charge times are 2311 s for $\epsilon = 0.6$, 2017 s for $\epsilon = 0.68$ and 1796 s for $\epsilon = 0.8$. In each case 2 min at zero current were simulated before discharge. See Tables 2–5 for the other parameter values.

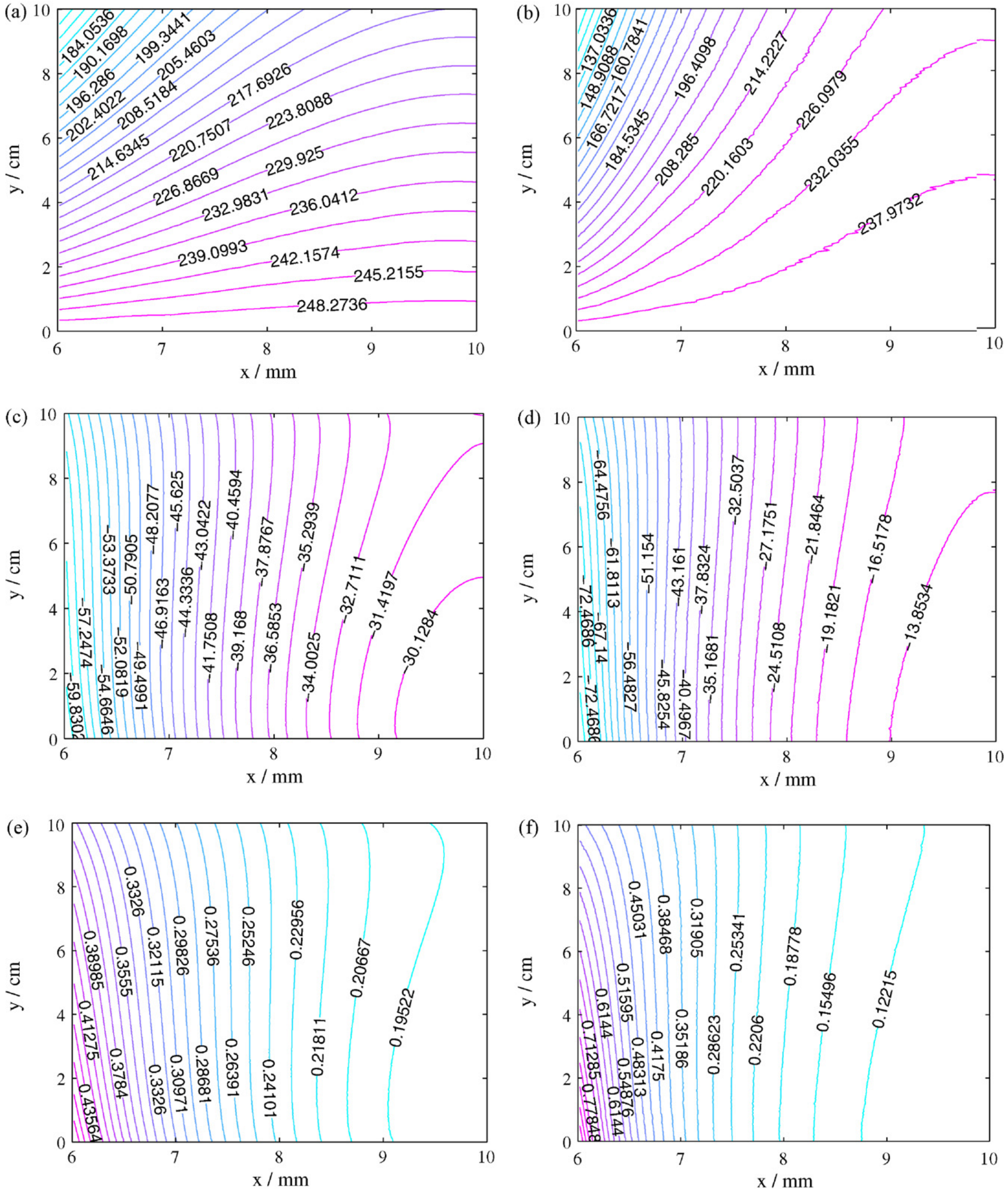

Fig. 11. Simulated contours of V(III) concentration at $t = 2311$ s for $\epsilon = 0.6$ and $t = 1796$ s for $\epsilon = 0.8$ (corresponding to the same state of charge) with $c^0_{\mathrm{III}} = 1080\,\mathrm{mol\ m^{-3}}$. Referring to Fig. 1, the line $x_1 = 6$ mm represents the current-collector/electrode interface and $x_2 = 10$ mm represents the membrane/electrode interface. Compare with the equivalent contour plots in Fig. 3.

5. Summary and future development

In this paper we have developed a modelling framework for the vanadium RFB, which can easily be extended to several other RFB types that employ an ion-exchange membrane. The foundations of the model are the fundamental laws of charge, mass and momentum conservation, and it therefore has the potential to predict performance in idealized scenarios. Comparisons between the simulation results and experimental data have demonstrated a good degree of accuracy in predicting the trends observed in a laboratory test, with respect to variations in two key parameters (concentration and flow rate). Further simulations have predicted that decreasing the electrode porosity by a relatively small amount can lead to a substantial increase in coulombic efficiency and a decrease in the rates of hydrogen and oxygen evolution.

One of the main benefits of the model when used in conjunction with experiment is the ability to predict, amongst other quantities of interest, profiles of concentration, overpotential and current density, as in Figs. 3–6. In situ experimental measurements of these quantities are extremely difficult to obtain, and in some cases impossible, yet this information (such as the likelihood of localized reactant depletion or of a steep potential rise) can be of vital importance to ensuring both good performance and longevity of the battery. To serve as a predictive tool the model would of course require extensive validation and possibly the inclusion of additional physical phenomena.

The current model can be extended in several respects. Temperature variations (in particular from heat loss) could play a significant role if there exists a steep temperature gradient between the battery and its surroundings, such as in a sub-zero environment. Such gradients would affect the reaction rates and material conductivities; the conductivity of a Nafion® membrane for example is highly sensitive to temperature. Another important feature of the real operation is the presence of side reactions, particularly hydrogen and oxygen evolution, which affect performance and lead to degradation of the electrode materials. Both temperature variations and side reactions will be considered in a forthcoming paper.

Appendix A. Nomenclature

a	geometric area of collector (m^2)
A	specific surface area of porous carbon electrode (m^{-1})
b	reverse reaction rate constant
c	concentration (mol m^{-3})
d	inter-fibre distance (m)
d_f	mean fibre diameter (m)
D	diffusion coefficient ($m^2\,s^{-1}$)
E	cell voltage (V)
E_0	open circuit voltage (V)
F	Faraday's constant (C mol^{-1})
h	electrode height (m)
$\vec{i}$	current density (A m^{-2})
I	current (A)
k	permeability (m^2)
k_i	reaction rate constants ($i = 1, 2$) (m s^{-1})
K	Kozeny-Carman constant
L	thickness/width (m)
$\vec{n}$	unit outer normal
$\vec{N}$	molar flux (mol $m^{-3}\,s^{-1}$)
p	pressure (Pa)
R	universal gas constant (J $mol^{-1}\,K^{-1}$)
S	source/sink (mol $m^{-3}\,s^{-1}$)
t	time (s)
T	temperature (K)
$\vec{v}$	velocity (m s^{-1})
V_T	electrolyte volume (half-cell) (m^3)
x	thickness (m)
y	height (m)
z	valence

Greek letters

α	transfer coefficient
γ	piston velocity (m s^{-1})
ϵ	volume fraction
η	overpotential (V)
κ	ionic conductivity (S m^{-1})
μ	dynamic viscosity (kg $m^{-1}\,s^{-1}$)
σ	electronic conductivity (S m^{-1})
ϕ	protonic potential (V)
ψ	electronic potential (V)
ω	volumetric flow rate ($m^3\,s^{-1}$)

Subscript

a	positive electrode quantity
av	average value
c	negative electrode quantity
coll	current collector quantity
e	electrolyte quantity
f	fixed charge quantity
H_2O	water property
i	species $i \in \{V(II), V(III), V(IV), V(V), H_2O, H^+, HSO_4^-, SO_4^{2-}\}$
in	inlet value
k	reaction (1) or (2)
s	solid or electronic property
w	water property (membrane)
0	initial or equilibrium value
$-$	negative electrode quantity/property
$+$	positive electrode quantity/property

Superscript

eff	effective value
in	inlet value
out	outlet value
0	initial value

References

[1] C.P. de Léon, A. Frías-Ferrer, J. González-Garcia, D. Szánto, F. Walsh, J. Power Sources 160 (2006) 716.
[2] M. Skyllas-Kazacos, C. Menictas, Proceedings of the INTELEC Conference, Melbourne, 1997.
[3] The VRB energy storage system: A comparison with lead acid batteries, Technical report, VRB Power Systems Inc, http://www.vrbpower.com/docs/whitepapers/, 2007.
[4] The VRB energy storage system: The multiple benefits of integrating the VRB-ESS with wind energy, Case studies in MWH applications, Technical report, VRB Power Systems Inc, http://www.vrbpower.com/docs/whitepapers/, 2007.
[5] M. Skyllas-Kazacos, R. Robins, US Patent 849,094 (1986).
[6] E. Sum, M. Skyllas-Kazacos, J. Power Sources 15 (1985) 179.
[7] M. Skyllas-Kazacos, F. Grossmith, J. Electrochem. Soc. 134 (1987) 2950.
[8] J. Newman, W. Tiedemann, J. Electrochem. Soc. 144 (1997) 3081.
[9] C. Wang, W. Gu, B. Liaw, J. Electrochem. Soc. 145 (1998) 3407.
[10] C. Wang, W. Gu, B. Liaw, J. Electrochem. Soc. 145 (1998) 3418.
[11] M. Doyle, T. Fuller, J. Newman, J. Electrochem. Soc. 140 (1993) 1526.
[12] T. Fuller, M. Doyle, J. Newman, J. Electrochem. Soc. 141 (1994) 1.
[13] T. Evans, T.V. Nguyen, R. White, J. Electrochem. Soc. 136 (1989) 328.
[14] C. Fabjan, et al., Electrochim. Acta 47 (2001) 825.
[15] M. Gattrell, et al., J. Electrochem. Soc. 151 (2004) 123.
[16] J. Newman, Electrochemical Systems, Prentice Hall, Engelwood Cliffs, NJ, 1991.
[17] C.-Y. Wang, Chem. Rev. 104 (2004) 4727.
[18] A. Weber, J. Newman, Chem. Rev. 104 (2004) 4679.
[19] A. Kulikovsky, Electrochem. Commun. 4 (2002) 318.
[20] Z. Wang, C.-Y. Wang, K. Chen, J. Power Sources 94 (2001) 40.
[21] D. Bernadi, M. Verbrugge, AIChE J. 37 (1991) 1151.
[22] D. Bernadi, M. Verbrugge, J. Elecrochem. Soc. 139 (1992) 2477.
[23] R. Probstein, Physicochemical Hydrodynamics, Butterworth Publishers, MA, 1989.
[24] B. Bird, W. Stewart, E. Lightfoot, Transport Phenomena, 2nd ed., John Wiley and Sons, NY, 2002.
[25] R. Freeze, J. Cherry, Groundwater, Prentice-Hall, New Jersey, 1979.
[26] Y. Wang, C.-Y. Wang, Electrochim. Acta 50 (2005) 1307.
[27] T. Springer, T. Zawodinski, S. Gottesfeld, J. Elecrochem. Soc. 138 (1991) 2334.
[28] A. Weber, J. Newman, J. Elecrochem. Soc. 151 (2004) 311.
[29] A. Weber, J. Newman, J. Elecrochem. Soc. 150 (2003) 1008.

[30] T. Mohammadi, S. Cheng, M.S. Kazacos, J. Membr. Sci. 133 (1997) 151.

[31] M. Pourbaix, Atlas of Electrochemical Equilibria in Aqueous Solutions, second ed., NACE International, Houston, 1974.

[32] T. Yamamura, M. Watanabe, T. Yano, Y. Shiokawa, J. Elecrochem. Soc. 152 (2005) 830.

[33] R. Mills, Phys. Chem. 77 (1973) 685.

[34] M. Verbrugge, R. Hill, J. Elecrochem. Soc. 137 (1990) 886.

[35] G. Zaikov, A. Iordanskii, V. Markin, Diffusion of Electrolytes in Polymers, VSP, Utrecht, Netherlands, 1988.

[36] J. Brown, Tappi J. 33 (1950) 130.

[37] J. Fales, N. Vandeborough, Electrochem. Soc. Proc. 86 (1986) 179.